PCCP

ROYAL SOCIETY OF CHEMISTRY

PAPER

View Article Online
View Journal | View Issue

Cite this: *Phys. Chem. Chem. Phys.*, 2026, **28**, 10169

Quantitative analysis of FAI-diffusion in sequentially evaporated $FAPbI_3$ perovskite thin films

Tobias Schulz, [a] Matthias Maiberg, [a] Marcel Schrader,[a] Roland Scheer [a] and Paul Pistor *[b]

Physical vapor deposition of perovskite solar cells is gaining increasing importance due to its up-scaling potential applicability for the industrial manufacturing. Especially the layer-by-layer sequential approach allows for a more precise process and stoichiometry control and offers cross-contamination free deposition. However, a detailed analysis of perovskite film formation and growth is usually only done qualitatively, with a limited number of studies addressing this aspect. We want to start filling the gap of lacking quantitative evaluations by investigating the phase evolution inside the PbI_2–FAI diffusion couple during deposition and annealing with an *in situ* X-ray diffraction (XRD) system. The observed diffraction intensity transients allow us to calculate the diffusion coefficient of the diffusing species for different isothermal annealing temperatures. With a derived Arrhenius plot, the activation energy and pre-exponential factor for the diffusion constant is determined. This report describes the mathematical model underlying the evaluation as well as application to a PbI_2–FAI (FA^+: formamidinium $CH(NH_2)_2^+$) diffusion couple, *i.e.* two initially separated layers brought into contact, enabling interdiffusion and reactive perovskite formation upon annealing. We find a linear trend in the Arrhenius plot, resulting in an activation energy of 0.83 eV. A variation of the initial parameters shows only minor activation energy changes, indicating a robust underlying mathematical model.

Received 25th August 2025,
Accepted 20th March 2026

DOI: 10.1039/d5cp03252k

rsc.li/pccp

1. Introduction

The first successful introduction of organo-metal-halide perovskite solar cells (PSCs) into the field of photovoltaics in 2009[1] came along with a huge rise of attention for this material class. In the following years many techniques to prepare the PSCs got invented with spin-coating yielding the, to date, highest power conversion efficiency (PCE) of 27.0%.[2] However, this preparation method bears several disadvantages like the insufficient upscaling potential[3,4], low material yield and the usage of environmental-toxic solvents.[5,6]

A solvent-free alternative are vacuum-based deposition techniques such as physical vapor deposition (PVD). In this field Snaith *et al.* are the pioneers with their co-evaporated $MAPbI_{3-x}Cl_x$ (MA^+: methylammonium $CH_3NH_3^+$) solar cell (PCE of 15.4%).[7] However, controlling the perovskite stoichiometry is challenging for co-evaporated absorbers due to inevitable fluctuations of material fluxes reaching the substrate. A more precise stoichiometry control can be achieved *via* sequential layer-by-layer deposition of each individual precursor.[5,8] Additionally, sequential thermal evaporation of the organic ammonium salts and lead halides allows the deposition of both species in separated vacuum chambers, reducing cross-contamination.[8,9] Using this technique Li *et al.* recently reached a PCE of 24.42% for $Cs_{0.05}FA_{0.95}PbI_3$[8]. For sequentially evaporated PSCs, material diffusion, which is driven by concentration gradients, is a key process. However, there are only few publications about sequentially evaporated PSC and only limited knowledge concerning the concentration-driven ionic diffusion kinetics during the annealing step exists.

In contrast to the concentration-driven diffusion, investigations of the ionic drift due to an external electric field already exist since 2015. At this time Tress *et al.*[10] proposed the idea, that the *J*–*V*-hysteresis effect could originate from the existence of mobile ions within the $MAPbI_3$ perovskite absorber. This assumption was theoretically verified by Haruyama *et al.*[11] using density functional theory (DFT) calculations for $MAPbI_3$ and $FAPbI_3$. They also determined the activation energies for the ionic drift of I^-, MA^+, and FA^+ ions to be 0.44–0.48 eV, 0.57 eV and 0.61 eV, respectively. An experimental verification

[a] *Martin-Luther-University Halle-Wittenberg, Von-Danckelmann-Platz 3, 06120 Halle, Saale, Germany*
[b] *Center for Nanoscience and Sustainable Technologies (CNATS), Department of Physical, Chemical, and Natural Systems, Universidad Pablo de Olavide (UPO), Carretera de Utrera 1, 41013 Sevilla, Spain. E-mail: ppis@upo.es*

was published by Eames *et al.*[12] using chronophotoampereometry measurements. In their work the activation energies for I^- and MA^+ ion drift in $MAPbI_3$ were calculated to be 0.58 eV and 0.84 eV, leading to comparable values to Haruyama *et al.* Also, the ionic drift activation energy of Pb^{2+} ions was determined as 2.31 eV, indicating a neglectable diffusion of the metal ion and a rather stable PbI_2 framework. In 2019 Futscher *et al.*[13] conducted a deeper analysis of ion migration in $MAPbI_3$ perovskites using transient capacitance measurements. They were able to not just calculate the activation energies (0.29 eV for I^- and 0.39–0.90 eV for MA^+) but also the ion density and diffusion coefficient (at 300 K). For I^- they calculated 3.1×10^{-9} cm^2 s^{-1} and 1.6×10^{-12}–6.8×10^{-12} cm^2 s^{-1} for MA^+, respectively. Furthermore, the comparable slower MA^+ ion diffusion was assigned to be the origin of the *J–V*-hysteresis effect, while the I^- ions relax too fast to have a significant effect on the *J–V* curves.

As already mentioned, knowledge about activation energies and diffusion coefficients for concentration-driven diffusion is still underexplored. To fill this gap, we conducted systematic experiments to evaluate the kinetics of the diffusion-reaction mechanisms of sequentially evaporated PbI_2 and FAI films and their diffusion/reaction kinetics during annealing. For that purpose, we prepared $FAPbI_3$ films *via* sequential thermal evaporation of PbI_2 and FAI and subsequently annealed the layer stack in the same vacuum chamber (see Fig. 1). The vacuum chamber is equipped with an *in situ* X-ray diffraction (XRD) set up that allows to monitor the evolution of the crystalline phases within the film in quasi real-time. After depositing PbI_2 and FAI we subjected the layer stack to a series of different isothermal annealing conditions, while recording the X-ray diffraction patterns of the evolving film. By comparing the diffusion kinetics of layer stacks isothermally annealed at different temperatures, we were able to extract the kinetic parameters for this process and generate a holistic diffusion model approach, allowing us to determine the diffusion coefficient for different temperatures and from this the activation energy. For the verification of the model we also performed SEM measurements and determined the final film thickness and morphology. Finally, an error estimation of the calculated diffusion coefficients and activation energy is conducted.

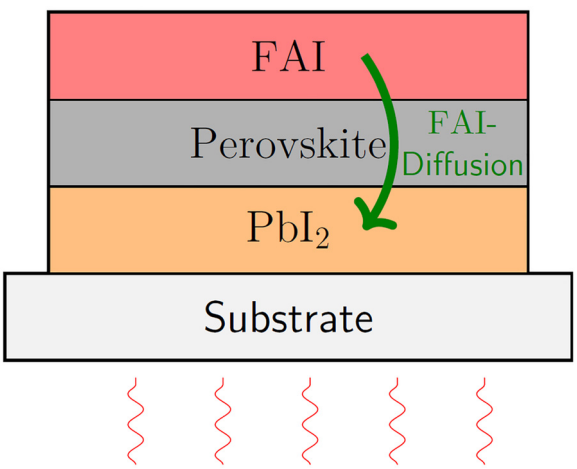

Fig. 1 Schematic illustration of the used PbI_2–FAI diffusion couple, with the perovskite growing between them during the annealing.

2. Experimental section

2.1 Substrates

For all experiments, we used commercial glass substrates coated with ITO (100 nm) provided by KINTEC. The cleaning of the coated substrates was performed in three steps using an ultrasonic bath. In the first step we used a cleaning soup with water and 1% EMAG EM-080, followed by isopropyl alcohol (IPA) and acetone for 15 min each. After cleaning we spin-coated the hole transport layer (HTL) poly[bis(4-phenyl)(2,4,6-trimethylphenyl)amine] (PTAA). For that a solution of 2.5 mg ml^{-1} in toluene was used. The samples were then transferred to a glove box, which is directly attached to our vacuum chamber.

2.2 Perovskite formation

The source materials for evaporation, PbI_2 (99.999%, Thermo Scientific) and FAI (>99.99%, Greatcell), were stored in the attached glove box and were used as received. These materials were sequentially deposited *via* thermal evaporation onto the glass-ITO-PTAA substrate. Firstly, PbI_2 was evaporated (645 nm, 0.5–0.8 Å s^{-1}, 6.16 g cm^{-3} (ref. 14)) and subsequently FAI (1200 nm, 1.0–2.0 Å s^{-1}, 2.48 g cm^{-3} (ref. 15)). The deposited amount of each reactant was monitored by a quartz crystal microbalance (QCM) and by laser light scattering (LLS). During the deposition the substrate temperature was 25 °C. An example of the *in situ* XRD data obtained, as well as the explanation of the LLS technique, is given in Fig. S1 and the corresponding paragraph in the SI. It is important to note, that the temperature reading during the following annealing step is done on the back side of the sample, where the heating element is placed, leading to a discrepancy between nominal (back side) and real (front side) temperature. We performed experiments with self-adhesive temperature labels to estimate the real temperature on the front side, where the material stack is located. In Fig. S4 a photograph of these labels (front side temperature) is shown together with the nominal back side temperature. Based on this, we estimate the temperature difference in the chosen temperature range (90–120 °C) to be around 16 °C (see SI). This will be considered when the Arrhenius graph is plotted, but in the following, the experiments will still be labelled with respect to the nominal back side temperature. The sequential deposition results in a FAI/PbI_2 double layer stack of around 2000 nm total thickness. The FAI film thickness was chosen about twice as thick as the PbI_2 layer with a 2 : 1 FAI : PbI_2 particle ratio to guarantee a quasi-infinite FAI material source (see section "Derivation of Diffusion Model"). The vacuum chamber has a base pressure of 2×10^{-5} mbar and a maximum operational pressure of 1×10^{-4} mbar. Monitoring of the pressure was done with an Edwards WRGS-NW35 wide range gauge.

2.3 XRD measurements

During evaporation and annealing, XRD *in situ* measurements were performed, where the entering/exiting X-rays passed through Kapton windows installed in the evaporation chamber walls. The Kapton windows were replaced after each process in order to reduce absorption of X-rays by deposited material. For the *in situ* XRD, Cu-K_α radiation (wavelength 1.54 Å) from an X-ray tube with a power of 1.6 kW (40 kV, 40 mA) was used. The K_β radiation was attenuated *via* a Ni-filter to 5% of the K_α intensity. The setup is capable of measuring one XRD scan with an angular range of 28° every 120 s with a linear detector array consisting of three Dectris Mythen 1 K modules. Because of the three individual detector modules, two small detector gaps arise in the measured diffractograms. During *in situ* measurements, the setup uses a fixed source-detector ω (incident) and Ω (detector) geometry. In all experiments $\omega = 9°$ and $\Omega = 13°$ were used. Only diffraction peaks, which have the same incident and outgoing angle (θ–2θ condition) are in the focus point of the goniometer circle. All other diffraction peaks are out of focus and thus have a larger full width at half maximum (FWHM). The experiments were conducted at constant annealing temperatures. A more detailed description of the *in situ* XRD setup can be found in ref. 16–19. One scan was performed accumulating the diffraction intensity for the period of 120 s. Between the scans there is a downtime of 2 s for data transfer. This downtime is considered in the time stamp of the experiment. Fig. 2 shows exemplarily the *in situ* XRD data for the annealing process at 100 °C in a colormap representation. The remaining colormaps of the other annealing temperatures can be found in the SI. In Fig. 3, a qualitative comparison of the different diffusion/reaction kinetics for different isothermal annealing (initial heating takes 10 min) temperatures in the temperature range between 90 °C and 120 °C is shown for one characteristic $FAPbI_3$ perovskite peak. With these experiments, we can show that: (i) a complete conversion from the FAI/PbI_2 layer stack is possible (extinction of the FAI and PbI_2 peaks). (ii) The time for the diffusion/reaction and perovskite formation to be completed decreases from about roughly 200 min (at 90 °C annealing) to roughly 50 min (at 120 °C annealing). The integrated peak intensities were fitted with the program PDXL version 2.8.1.1 by Rikagu Inc. using a split pseudo-Voigt line profile. The evolution of the diffraction patterns provides us with a time-resolved information of the different crystal phases involved, and in the integrated intensities of their characteristic peaks lies the information of how much of this phase is present (basically the film thickness in a one-dimensional diffusion model). To minimise the influence of different preferred orientations, a weighted sum over all detectable PVK reflections was applied. This procedure and the analysis of the XRD intensities is explained in more detail later on.

2.4 Film characterisation

To determine the final film thickness after each experiment SEM cross-section measurements were performed with a Zeiss Supra 40 VP. A secondary electron in-lens detector and an acceleration voltage of 5 kV was used. The SEM device is also equipped with a Bruker EDX detector. EDX measurement were performed using an acceleration voltage of 15 kV, a working distance of 6 mm and a magnification of 500. For quantification L-lines of iodine and M-lines of lead were used. Background correction and quantitative analysis were performed using a standardless method based on the ratio of peak intensity to background signal, combined with atomic number, absorption, and fluorescence correction ((P/B) ZAF fitting).

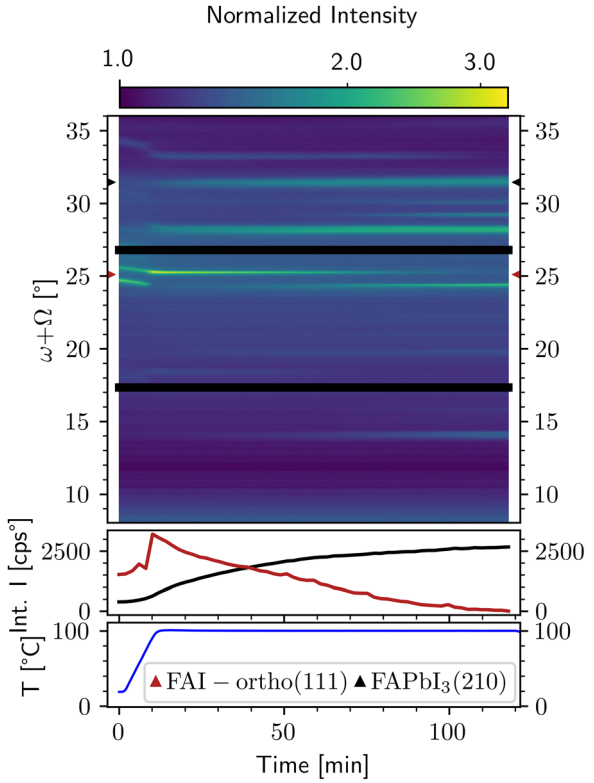

Fig. 2 The top graph shows a color plot representing the normalized color coded diffraction intensity as a function of diffraction angle (y-axis) and time (x-axis). Example of annealing an PbI_2/FAI stack at 100 °C. The middle graph shows the integrated intensities in counts per second of the 111 peak at 25.1° of orthorhombic FAI (red) and the 210 peak at 31.4° of cubic $FAPbI_3$ (black). The bottom graph displays the evolution of the substrate temperature.

3. Derivation of diffusion model

In this section, the diffusion model we use to determine the diffusion coefficient D based on the *in situ* XRD data is explained. The standard approach for determination of diffusion coefficients is to measure concentration depth profiles with methods like glow discharge optical emission spectroscopy (GDOES)[20] or secondary ion mass spectroscopy (SIMS).[21] Both methods rely on sputtering through the sample. The GDOES technique has two major downsides. On the one hand, a reliable surface analysis is not achievable due to the initial building up of the plasma. On the other hand, controlling the shape of the sputter crater is difficult resulting in an increasing

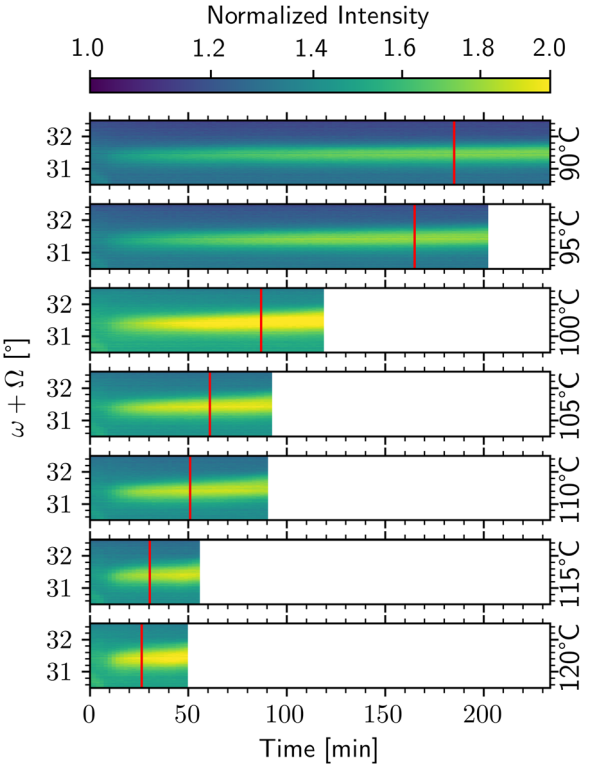

Fig. 3 *In situ* diffractograms of the 3D 31.4° peak for all nominal temperatures. The red line indicates the adjusted t_{end}. A gradually decreasing necessary annealing time is needed with increasing annealing temperature.

error with sputtering time. The major downside of SIMS is the so-called "matrix effect". This effect leads to a different amount of ejected particles based on the underlying layers, making quantifications rather complex. As an alternative, we used *in situ* XRD to analyse the diffusion-reaction kinetics of the sequentially deposited perovskite layer stacks. XRD probes the bulk, and in this work, we consider integrated XRD peak intensities (peak areas) as proportional to the amount of a crystalline phase in the sample. Applying a diffusion model and fitting procedure to the time-dependent data of the *in situ* XRD measurements for a set of different isothermal annealing temperatures T allows us to extract the temperature dependent diffusion coefficient $D(T) = D_0 \times \exp(-E_a/(k_B T))$, where D_0 is the preexponential factor, E_a the activation energy, and k_B the Boltzmann constant. The following section will describe the experiment and derive a model to determine these diffusion coefficients and explain the technical and physical uncertainty sources like the intensity dependence from the ω (incident) and Ω (detector) angles, attenuation effects, and the coexistence of multiple perovskite phases, namely lower and higher dimensional perovskites (LDP and HDP).

3.1 Description of experiments and XRD analysis

To investigate perovskite formation, we sequentially deposited the reactants PbI_2 and FAI on glass/ITO/PTAA substrates at room temperature in the first step (deposition). This process step was identical for all experiments, and the *in situ* XRD data representation of all depositions is presented as colormaps is in the SI, verifying the reproducibility of this process step (see Fig. S1 and S2).

In a following isothermal annealing step, the different species interdiffuse and a perovskite phase is formed. Fig. 2 shows exemplarily the *in situ* diffractogram of the annealing step for an experiment with a nominal isothermal annealing temperature of 100 °C (upper part). In these colormaps, the abscissa shows time, the ordinate the diffraction angle $\omega + \Omega$ and the XRD intensity is color coded. In other words, in this data representation, each column corresponds to one XRD scan with an accumulation time of 120 s. For all experiments an angle of incidence of $\omega = 12°$ was chosen, bringing the $\omega + \Omega$ region around 24° in the parafocus. Hence, all evaluated peaks are not too far from that focus condition and the resulting peak broadening is minimized. The 2 black regions in the colormaps stem from the before mentioned spatial gaps between the 3 detector modules. In the *in situ* diffractograms no K_β signals are shown. The used Ni filter reduces the K_β intensity to approximately 5% of the corresponding K_α signal. To correct for this residual K_β contribution, 5% of the K_α intensity was subtracted from the measured intensity at each angle. The bremsstrahlung background is not subtracted. The middle graph shows the evolution of the integrated intensities of two characteristic Bragg reflexes, namely of the (111) peak of orthorhombic FAI (red) at 25.1° (ref. 15) and the (210) peak of cubic $FAPbI_3$ (black) at 31.4°.[22] Fig. S6 in the SI gives the same plot, but with labelling all detectable peaks. Please note, that with the chosen detector setting, no PbI_2 peaks are detected, even during/after the deposition process, as is detailed in the SI. The bottom graph shows the substrate temperature. It is seen, that after around 10 min the desired nominal temperature of 100 °C is reached. In the upcoming sections the integrated intensities of several perovskite and FAI peaks are used to determine the diffusion coefficients. For that, Fick's second law is used to simulate the particle flux J, which is necessary for simulating the integrated XRD intensities. By comparing these intensities with the measured data, we calculate the diffusion coefficient for each isothermal experiment. In order to form the diffusion system, first a PbI_2 layer and afterwards a FAI layer was deposited onto a glass/ITO/PTAA substrate. At the interface between the reactants PbI_2 and FAI the perovskite is forming, and therefore the diffusion system to be considered is PbI_2/Perovskite/FAI.

3.2 Assumptions and preconditions

Depending on their diffusion constants, both reactants PbI_2 and FAI in principle can each diffuse through the perovskite towards the other reactant layer. However, a well-known fact from literature as well as from our own studies[18,23] is that in this specific stack mainly the FAI is diffusing while PbI_2 is not diffusing or only to a minor degree. This forms the first assumption or precondition of the following evaluation. Interestingly, it was found, that without voltage bias the FAI is diffusing as a complete molecule and not in dissociated form.

For dissociative FA^+ and I^- diffusion, the presence of humidity is required.[23] A second assumption of the upcoming evaluation is that the diffusion only occurs in one dimension, perpendicular to the substrate plane. In Fig. S8, a SEM cross-section of a PbI_2–FAI film directly after deposition and before annealing is shown. Here, a clear interface with little interface roughness between both reactants is seen. This supports our assumption of a one-dimensional diffusion system. Thirdly, semi-infinite FAI and PbI_2 layers are assumed to ensure constant boundary conditions (see Mathematical ansatz chapter). This means that our model is only valid until one of the reactant layers is completely consumed.

A fourth assumption for the model is that FAI species instantaneously react to perovskites as soon as FAI arrives at the PbI_2|perovskite interface and encounters free PbI_2 species. This assumption excludes the existence of FAI species within the PbI_2 layer. Further, it encompasses that in the specific stack PbI_2|FAI the perovskite growth is diffusion-controlled and not reaction controlled. The instantaneous reaction of FAI particles makes the PbI_2 layer a sink for FAI, but with a moving boundary. Both reactants are consumed during the reaction and the perovskite thickness is increasing.

Another important point is that not only the ordinary cubic 3D perovskite $FAPbI_3$ is formed during the annealing step, but also lower dimensional perovskites (LDP), for example the 2D perovskite FA_2PbI_4 (2D) or perovskites with even lower dimensions. A more detailed analysis of all existing phases during our experiments will be given in Section 4. In this evaluation, we do not differentiate between different diffusion coefficients in the different PVK phases but rather derive an effective value over all phases. In the following we will refer to the product layer consisting of all possible perovskite dimensionalities as the "perovskite" or "PVK" layer.

Furthermore, we assume a concentration independent diffusion coefficient, making it a constant value within the perovskite layer, independently of the dimensionality.

Next, an assumption regarding the depth-dependent concentration profile of the diffusing FAI particles is necessary. A schematic representation of the concentration profiles at different times is shown in Fig. 4. As already described above, within the PbI_2 layer no FAI can exist due to the "instantaneous" formation of FAI and PbI_2 to $FAPbI_3$ at the beginning of the diffusion process (which here actually starts to some extent already at room temperature during the deposition of FAI) only FAI and PbI_2 are present. We can define the concentration of FAI (particles per volume) within the FAI-layer as c_0. This value is calculated *via* the unit cell volume of FAI (461.06 $Å^3$) and the number of FAI particles (formula unit Z) within this volume (4 particles)[15] to 14.36 mmol cm^{-3}. As soon as some perovskite has formed (independent of the dimensionality) a certain FAI concentration gradient will form inside the perovskite layer. From the FAI side, FAI molecules will diffuse into the perovskite. At the perovskite|PbI_2 interface, FAI molecules will diffuse out of the perovskite and form new perovskite. Therefore, at the FAI|PVK interface the FAI concentration will be highest, and then gradually decrease within the perovskite towards the PVK|PbI_2 interface. Here, two boundary conditions are of importance: there is a maximum amount of FAI (molar concentration) that can exist within the perovskite film, the saturation concentration c_s. It is important to recall, that "perovskite" includes not just the ordinary 3D $FAPbI_3$, but also all LDPs. At the FAI|PVK interface the concentration of FAI will amount to this value. In the following, we present two approaches on how to derive this saturation concentration c_s.

For the experimental determination of c_s, we conducted a simple experiment where FAI is deposited on a heated substrate with an already deposited PbI_2 layer. The increased substrate temperature prevents FAI accumulation on top of the PbI_2 layer due to immediate interdiffusion and PVK formation. The FAI deposition continues until the first traces of a separate, crystalline FAI phase is detectable in the XRD. This marks the time, when no more FAI can be built into the PVK structure and FAI crystallizes as a second phase. Following EDX measurements allow to calculate the FAI : PbI_2 ratio for the moment that the first FAI peaks occurred. In Fig. 5 the experiment is shown. 60 nm of PbI_2 were evaporated on ITO/PTAA (ITO peak positions: 21.5, 30.6, and 35.4° (ref. 24)), afterwards the nominal substrate temperature was increased to 100 °C, then FAI was evaporated on the heated PbI_2 film. Due to the higher substrate temperature, the sticking coefficient of FAI on the substrate

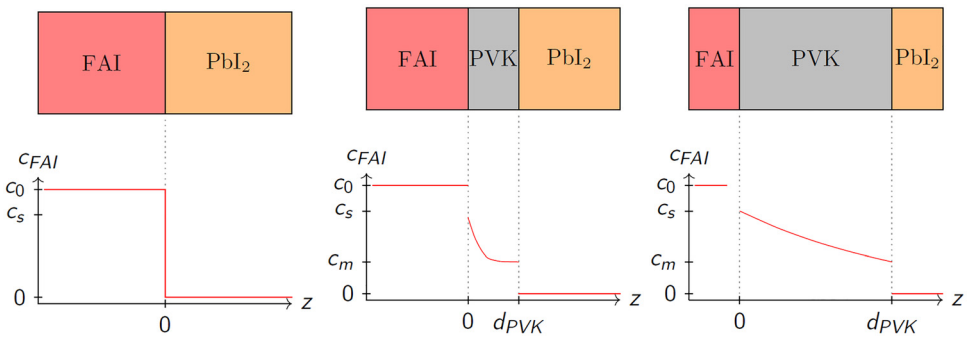

Fig. 4 Schematic concentration profiles for $t = 0$ (left), $t = t_0$ (middle), and $t > t_0$ (right). Inside the FAI and PbI_2 reactants, the FAI concentrations are constant at c_0 and 0, respectively. Within the perovskite a monotonuos decrease is assumed with c_s being the left and c_m being the right boundary condition at the interfaces.

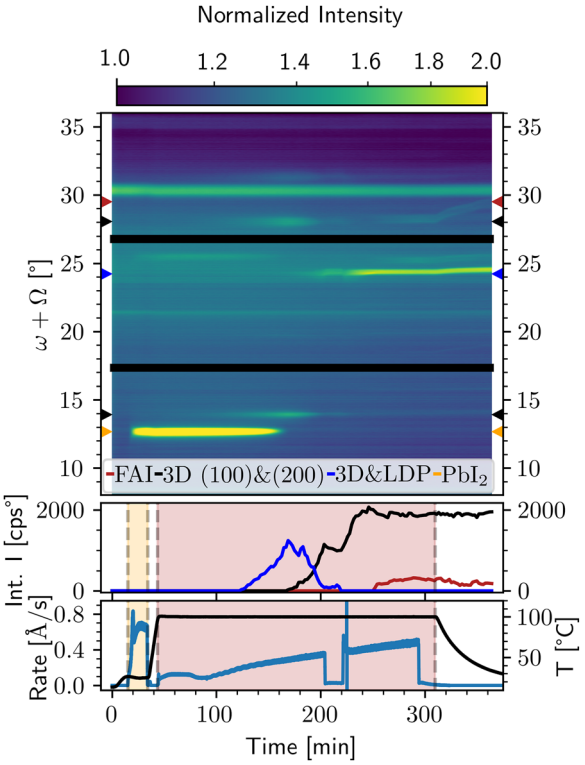

Fig. 5 *In situ* diffractograms of the saturation concentration determination experiment represented as a colormap. After depositing PbI_2, the substrate was heated to a nominal temperature of 100 °C and FAI got deposited. Up to 250 min, all FAI is incorporated into the PVK structure. After this time, a crystalline FAI secondary phase is forming. The peaks at 21.5°, 30.6°, and 35.4° are from the substrate (ITO).

reduces. This leads to a smaller deposition rate, but larger FAI diffusivity. After 100 min, the PbI_2 peak at 12.7° starts to decrease and the $FAPbI_3$ (100) and (200) peaks at 14° and 28° respectively start to increase. Upon further FAI deposition and diffusion, the 3D $FAPbI_3$ (100) and (200) peaks decrease again and a 3D (111) & LDP peaks at 24° start to appear. A clear distinction between the 3D (111) peak at 24.22°, the 2D (110) peak at 24.27°, and the 1D (104) peak at 24.07° is not possible due to their close proximity. This intensity change from mainly 14° and 28° to 24° signalises the transition from the ordinary 3D phase to LDP phases. We closed the FAI shutter after 200 min for 20 min to verify, that no FAI is piling up on the surface. As seen, the integrated intensities do not change during that time, suggesting the absence of a FAI layer, which would still keep diffusing into the layer in that time. After 220 min., the FAI shutter was reopened. After 250 min, a monoclinic FAI ($\bar{1}02$) peak at 28° starts to appear. This means, that at t = 250 min the saturation concentration of FAI in a PVK layer is reached. After closing the shutter a second time, the integrated intensities do not change again, indicating that no further FAI can be dissolved inside the PVK structure. The following EDX measurements result in an approximate FAI : PbI_2 ratio of 4 : 1 extrapolated to the time t = 250 min. We calculated the tooling factor for the deposition of FAI on the heated substrate to calculate back *via* QCM how much FAI was deposited until 250 min. The FAI : PbI_2 ratio of 4 : 1 is consistent with the ratio of a the 0D FA_4PbI_6 perovskite, which is the PVK phase with the lowest dimension (highest FAI content), so these results are consistent. Due to the lack of literature on that specific phase we cannot calculate the saturation concentration (as FAI particles per volume) for this 0D FA_4PbI_6 phase. To nevertheless estimate the saturation concentration, we can compare the FA-based system with the chemical similar MA-system. Here, Yokoyama *et al.* calculated the crystal structure for all dimensionalities, from 3D $MAPbI_3$ up to 0D MA_4PbI_6.[25] When calculating the saturation concentration of MAI in all these lattices (see Table S1), a monotonous increasing trend with decreasing dimensionality can be seen. This is also valid for the normalised saturation concentration c_s/c_0 ($c_{0,MAI}$ = 14.08 mmol cm^{-3}). In the FA-system, the normalised concentration ($c_{0,FAI}$ = 14.36 mmol cm^{-3}) for the 3D and 2D is similar to the MA-system. Because no structural information is known in the literature for the 1D FA_3PbI_5 and 0D FA_4PbI_6, we assume a similar trend of increased normalised concentration c_s/c_0. Following this route of thoughts, we assume a FAI normalised saturation concentration of c_s/c_0 of 80% as an upper limit, as in the MA-system.

For an alternative derivation of a lower limit for c_s, we can consider the 2D FA_2PbI_4, which we clearly detect in the *in situ* XRD, as the PVK phase with highest FAI content that we clearly detect in the XRD. As can be seen in Table S1 of the SI, the 2D FA_2PbI_4 phase has a relative saturation concentration c_s of 70%. With the hypothesis that this 2D phase will form at the FAI|PVK interface, the normalised saturation concentration then would read 70%. This leads to a normalised saturation concentration range of 70–80%. In the "Discussion" chapter the influence of the selected saturation concentration will be assessed.

The second important interface in the diffusion system is PVK|PbI_2. This interface defines the minimum concentration of FAI c_m, that is needed to grow a PVK. In literature as well as in our own studies[18,26], no PbI_2 rich phases for the FA-system exist. This results in 3D $FAPbI_3$ being the perovskite with the lowest FAI content. The calculated concentration of that phase (6.46 mmol cm^{-3}, 45%) marks the minimum concentration. Both, c_s and c_m, are important boundary conditions for our model.

3.3 Mathematical ansatz

After discussing the physical assumptions, the mathematical derivation is described. In a first step a numerical solution for the depth dependent concentration c of FAI within the PVK phase will be presented. In a second step the correlation between the measured XRD intensities and the concentration gradient will be discussed.

We start with Fick's second diffusion law

$$\frac{\partial c}{\partial t} = D \cdot \frac{\partial^2 c}{\partial z^2} \quad (1)$$

Here c describes the concentration of FAI within the PVK layer. D is the diffusion coefficient of FAI in the PVK layer, which here is assumed to be constant throughout the PVK layer and is not changing with time. t and z are the time and the

one-dimensional space coordinate, respectively. The coordinate system is chosen in the relative system of the PVK layer, such that the FAI|PVK interface is fixed to $z = 0$ and the PVK|PbI_2 interface is at $z = d_{PVK}$ (see Fig. 4), although for an external observer both interfaces are moving in opposite directions. We are thus looking for a solution to eqn (1) in the domain $0 \leq z \leq d_{PVK}$. To solve the partial differential equation (PDE) we need the following starting and boundary conditions, which derive from the assumptions in Section 3.2:

$$c(z > 0, t = t_0) = c_m \quad (2)$$

$$c(z = 0, t > t_0) = c_s \quad (3)$$

$$c(z = d_{PVK}(t), t > t_0) = c_m \quad (4)$$

Fick's law (1) together with the conditions (2)–(4) is a so called initial-boundary problem. More precise, it is an initial-boundary problem with inhomogeneous moving boundaries, since the position of the right boundary of the PVK layer depends on the (time dependent) perovskite thickness $d_{PVK}(t)$. The mathematical solution of such a moving boundary problem is not trivial and it is more convenient to transform it into an initial-boundary problem with homogeneous, fixed boundaries first. To this end, we first define a function $g(z,t) = \frac{c(z,t) - c_m}{c_s - c_m}$ for which we obtain

$$\begin{cases} \dfrac{\partial g}{\partial t} = D \cdot \dfrac{\partial^2 g}{\partial z^2} \\ g(z > 0, t = t_0) = 0 \\ g(z = 0, t > t_0) = 1 \\ g(z = d_{PVK}(t), t > t_0) = 0 \end{cases} \quad (5)$$

Now, the right boundary is homogeneous, but still moving in time. To fix it, we define a new function $f(z', t) = g(z' d_{PVK}(t), t)$, which realizes a scaling of the position axes. Problem (5) then becomes:

$$\begin{cases} \dfrac{\partial f}{\partial t} = d'_{PVK}(t) \times \dfrac{z'}{d_{PVK}(t)} \dfrac{\partial f}{\partial z'} + D \dfrac{1}{d_{PVK}(t)^2} \dfrac{\partial^2 f}{\partial z'^2} \\ f(z' > 0, t = t_0) = 0 \\ f(z' = 0, t > t_0) = 1 \\ f(z' = 1, t > t_0) = 0 \end{cases} \quad (6)$$

Here, the term $d'_{PVK}(t)$ describes the time derivative of the PVK layer thickness. Now we finally arrived at a system with fixed, homogeneous boundaries and standard numeric methods like finite differences can be applied. The original function $c(z, t)$ can then be obtained from $f(z', t)$ by

$$c(z,t) = (c_s - c_m) \times f\left(\frac{z}{d_{PVK}(t)}, t\right) + c_m \quad (7)$$

Eqn (6) shows, that the PDE requires the knowledge of the perovskite thickness time evolution. The thickness increase of the PVK layer, however, depends on the amount of FAI which arrives at the right PVK|PbI_2 interface. $d_{PVK}(t)$ must therefore be determined self-consistently with eqn (6). To this end, we first examine the thickness increase Δd_{PVK} within a small time step Δt and we can write

$$\Delta d_{PVK} = J_{PVK|PbI_2} \cdot V_{UC} \cdot N_A \cdot \Delta t \quad (8)$$

Here, V_{UC} and N_A describe the unit cell volume and Avogadro's constant, respectively. The FAI particle flux $J_{PVK|PbI_2}$ is calculated *via* Fick's first law, which by virtue of eqn (7) can be written as

$$J_{PVK|PbI_2} = -D \cdot \left.\frac{\partial c}{\partial z}\right|_{z=d_{PVK}} = -D \cdot \frac{c_s - c_m}{d_{PVK}(t)} \left.\frac{\partial f}{\partial z'}\right|_{z'=1} \quad (9)$$

Plugging eqn (9) into eqn (8) and performing a transition to infinitesimal time steps, leads to:

$$\begin{aligned} \frac{d}{dt} d_{PVK}(t) &= J_{PVK|PbI_2} \cdot V_{UC} \cdot N_A \\ &= -V_{UC} \cdot N_A \cdot D \cdot \frac{c_s - c_m}{d_{PVK}(t)} \cdot \left.\frac{\partial f}{\partial z'}\right|_{z'=1} \end{aligned} \quad (10)$$

This is a first order ordinary differential equation, whose solution can be computed to

$$\begin{aligned} d_{PVK}(t) \cdot \frac{d}{dt} d_{PVK}(t) &= \frac{1}{2} \frac{d}{dt} {d_{PVK}}^2(t) \\ &= -V_{UC} \cdot N_A \cdot D \cdot (c_s - c_m) \cdot \left.\frac{\partial f}{\partial z'}\right|_{z'=1} \end{aligned} \quad (11)$$

$$d_{PVK}(t) = \sqrt{{d_{PVK,0}}^2 - 2 \cdot V_{UC} \cdot N_A \cdot (c_s - c_m) \cdot \int_{t_0}^{t} D \cdot \left.\frac{\partial f}{\partial z'}\right|_{z'=1} dt'} \quad (12)$$

The equation system (6) now has to be solved by taking eqn (12) into account. To this end, we chose an iterative approach. For the first iteration a constant perovskite thickness equivalent to the starting thickness is used: $d^0_{PVK}(t) = d_{PVK,0}$. This is plugged into eqn (6) and a 0th approximation $f^0(z', t)$ to $f(z', t)$ is calculated by a finite difference method. This is then used, to calculate an updates thickness $d^1_{PVK}(t)$ *via* eqn (12). This procedure is repeated until sufficient convergence is reached. At the end of this first step, we have a self-consistent solution $d_{PVK}(t)$ and, by eqn (7), $c(z, t)$.

After knowing the concentration profile, the link to the measured XRD intensities can be derived. Therefore, the correlation between concentration $c(t)$ and the absolute number of FAI particles $N_{PVK|PbI_2}$, which diffuse through the PVK|PbI_2 interfaces in the time interval between t_0 and t, needs to be written. This is done by integration of the FAI particle flux J through the PVK|PbI_2 interface over time.

$$N_{PVK|PbI_2} = \int_{t_0}^{t} J|_{z'=1} dt' = -\int_{t_0}^{t} D \cdot \frac{c_s - c_m}{d_{PVK}(t')} \left.\frac{\partial f}{\partial z'}\right|_{z'=1} dt' \quad (13)$$

By utilizing eqn (13), the final equation for the simulated integrated PVK XRD intensity is:

$$I_{\mathrm{sim,PVK}} = I_0 - \lambda_{\mathrm{PVK}} \cdot \int_{t_0}^{t} D \cdot \frac{c_s - c_m}{d_{\mathrm{PVK}}(t')} \frac{\partial f}{\partial z'}\bigg|_{z'=1} \mathrm{d}t' \tag{14}$$

Here, we assume a direct proportionality between the measured integrated XRD intensity I and the number of FAI particles N, that diffuse through each interface. The proportionality factor λ_{PVK} is defined by the molar mass M and mass density ϱ of the perovskite (4.09 g cm^{-3}),[22] as well as the ratio between intensity and film thickness $\alpha = \frac{I}{d}$. A more detailed discussion of this proportionality can be found in the SI. As the annealing starts with a small amount of PVK already present at the beginning of the experiment, a starting intensity I_0 has to be considered.

Eqn (14) allows to fit the increase of the perovskite peak intensities during the annealing experiment. To simulate the FAI peak decrease, an analogous derivation can be performed by considering the FAI|PVK interface for the concentration gradient. This results in the following formulas:

$$J_{\mathrm{FAI|PVK}} = -D \cdot \frac{\partial c}{\partial z}\bigg|_{z=0} = -D \cdot \frac{c_s - c_m}{d_{\mathrm{PVK}}(t)} \frac{\partial f}{\partial z'}\bigg|_{z'=0} \tag{15}$$

$$N_{\mathrm{FAI|PVK}} = \int_{t_0}^{t} J|_{z'=0} \mathrm{d}t' = -\int_{t_0}^{t} D \cdot \frac{c_s - c_m}{d_{\mathrm{PVK}}(t')} \frac{\partial f}{\partial z'}\bigg|_{z'=0} \mathrm{d}t' \tag{16}$$

$$I_{\mathrm{sim,FAI}} = I_0 - \lambda_{\mathrm{FAI}} \cdot \int_{t_0}^{t} D \cdot \frac{c_s - c_m}{d_{\mathrm{PVK}}(t')} \frac{\partial f}{\partial z'}\bigg|_{z'=0} \mathrm{d}t' \tag{17}$$

Our algorithm, which is based on the finite difference approach, is simulating a theoretical integrated intensity transient for a given set of c_s, c_m, and D and comparing it to the measured data *via* calculating the deviation Ω as

$$\Omega = \frac{1}{N} \sum_{j=1}^{N} \frac{|I_{\mathrm{XRD}} - I_{\mathrm{simulated}}|}{\max(I_{\mathrm{XRD}})} \tag{18}$$

With these equations the diffusion coefficients, which represent the data best, can be calculated. In the following section this will be shown exemplary on one diffusion experiment while for the other temperatures, we only give the extracted diffusion coefficients.

4. Results

This section will show exemplarily for the isothermal experiment at nominal 100 °C how a single isothermal annealing experiment is evaluated. The substrate reaches a nominal temperature of 100 °C after 10 min. During this heating phase the diffraction peaks at 24.7°, 25.6°, and 31.0° decrease drastically in intensity and new peaks arise at 25.1° and 32.8°. This indicates the transformation of FAI from the monoclinic to the orthorhombic phase.[15,27] The orthorhombic FAI peaks then decrease in intensity during the annealing experiment due to diffusion of FAI through the FAI|PVK interface to the PVK|PbI_2 interface, where they form new perovskite. As soon as an FAI particle crosses the FAI|PVK interface, it does not contribute to the FAI peak intensity anymore (see eqn (17)). The intensity decrease of the 25.1° (FAI 111) peak is shown in red in Fig. 2. Furthermore, a large number of peaks from PVK phases of all dimensionalities evolve during the annealing. These can be attributed to the 3D and 2D. For the 1D FA_3PbI_5 no literature data and thus no reference peak positions exist. However, a known phase is the 1D $(CI(NH_2)_2)_3PbI_5$ with an iodoformamidinium ($CI(NH_2)_2^+$ = iFA^+) cation instead of a formamidinium ($CH(NH_2)_2^+$ = FA^+) cation. The diffraction peaks attributed to that phase fit with our experimental data. We therefore assign this 1D $(iFA)_3PbI_5$ phase as one of our products in the perovskite layer, through which the FAI is diffusing.[28] The diffraction peaks, which are detectable in our experiments are: 13.8° (1D), 13.9° (3D), 19.7° (3D), 24.1° (1D), 24.2° (3D), 27.8° (1D), 28.0° (3D), 29.1° (1D), 30.0° (1D) and 31.4° (3D). Additionally, a 2D peak is located at 25.6°, which is in superposition with the orthorhombic FAI (111) peak, leading to a large fitting uncertainty. Because of that, this peak is not taken into consideration for the diffusion coefficient determination. Fig. S6 shows all mentioned peaks in the *in situ* diffractogram. Fig. S7 shows a diffractogram of the FAI and 2D PVK ($0\bar{1}3$) peak. All these PVK peaks are increasing in intensity during the annealing, indicating the formation of new PVK material. Since in the presented approach the XRD peak intensity is used for the quantification of the share of a certain phase, one has to exclude the influences of texture and grain reorientation. To this end, the weighted peak sum of all detectable PVK peaks was evaluated instead of single PVK peaks. For that, the peaks have been normalised according to the following formula:[29,30]

$$I_{\mathrm{PVK}} = \sum_{i=1}^{N} \frac{I_{\mathrm{XRD}}^{(i)}}{I_{\mathrm{rel}}^{(i)}} \tag{19}$$

with I_{rel} being the normalisation factor:

$$I_{\mathrm{rel}} = \mathrm{SCF} \cdot |F|^2 \cdot \mathrm{MU} \cdot G(\omega, \Omega) \cdot P(\omega + \Omega) \tag{20}$$

All constants and peak-independent parameters like initial intensity I_0 or detector sensitivity are combined in the scaling factor SCF. Also, the structure amplitude $|F|^2$, the multiplicity MU, geometric correction $G(\omega, \Omega) = \frac{1}{\sin(\omega) \times \sin(\Omega)}$, and polarisation term $P = 1 + \cos^2(\omega + \Omega)$ impact the resulting relative intensity. Here, ω and Ω describe the angle of incident and detector angle for the X-rays, respectively. Table S2 gives the values for all factors in eqn (20) for every used PVK peak.

In addition, we performed an experiment, where we co-evaporated $FAPbI_3$ and measured the integrated intensity of the PVK 24° peak (sum of 1D and 3D) in dependency of the deposited PVK thickness. In Fig. S10 it can be seen by the almost linear behaviour of the intensity vs thickness that for a film thickness below 2 μm, attenuation effects are neglectable. This verifies the direct proportionality $\alpha = \frac{I}{d}$ as stated in the previous section.

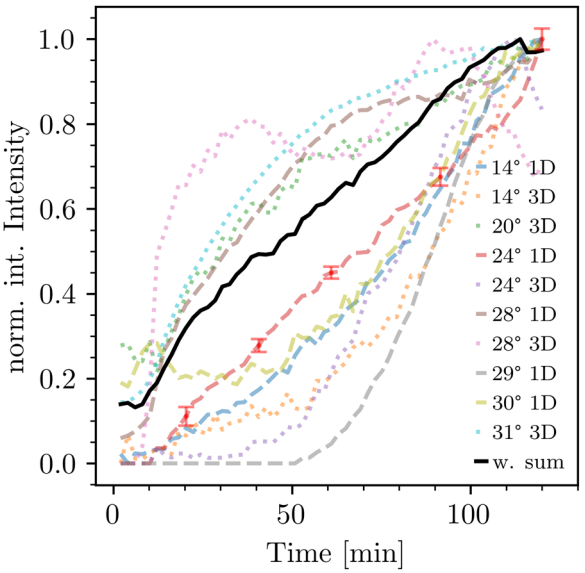

Fig. 6 Normalised integrated intensities of all visible PVK peaks as well as the weighted sum of all of them. All graphs are individually normalised. Dashed line represents all 3D peaks, dotted 1D, and full line shows the weighted sum. For the 1D peak at 24° some error bars are shown.

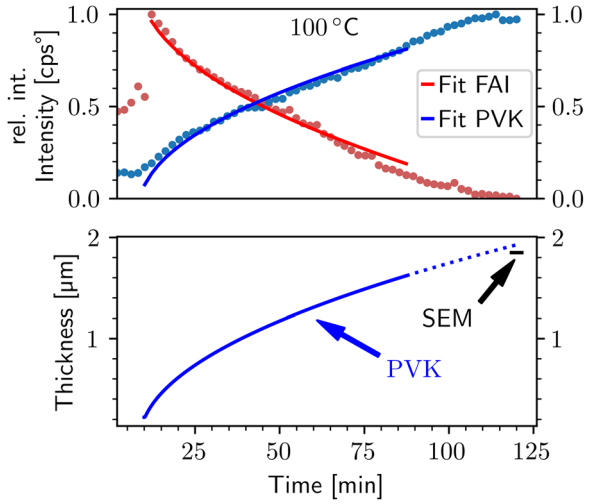

Fig. 7 Normalised measured data as well as simulated intensities for the FAI (111) peak and the weighted sum of all detectable PVK signals (top) and time dependent thickness of the PVK layer (bottom). t_{end} is set to 87.4 min. The resulting diffusion coefficient is $D = 4.66 \times 10^{-12}$ cm^2 s^{-1}.

Fig. 6 shows the $I(t)$ graphs for each normalised PVK peak as well as the weighted sum of all of them (black). Here we like to emphasize, that not every peak area evolution has the same shape. While the 3D peaks (dotted) mainly have a larger intensity increase at the beginning of the experiment, the 1D peaks (dashed) rise more towards the end of the annealing phase. For the weighted sum (black) a monotonous increasing integrated intensity is seen. Additionally, selected error bars from peak fitting are shown for the 1D PVK peak at 24° to demonstrate, that uncertainties arising from the fitting procedure are minor. For the following fitting procedure, only the weighted integrated intensity sum I_{PVK} will be used for the diffusion product. Additionally, the orthorhombic (111) FAI peak is evaluated as the reactant phase. For the fitting, a starting time t_0 of 10 min was chosen, after which the desired temperature (here nominal 100 °C) is reached. Additionally, within these 10 min the phase transition from monoclinic to orthorhombic FAI occurs, which explains the jump in the I_{FAI} data. In order to fulfil the assumption of a semi-infinite FAI source, the end time for the fitting is set to the time where the simulated FAI intensity falls to 10% of the initial intensity, which is after 87.4 min (t_{end}). The saturation concentration c_s and minimum concentration c_m are 11.49 mmol cm^{-3} and 6.46 mmol cm^{-3} respectively. Also needed are the initial ($d_{PVK,0}$) and the final (d_{SEM}) PVK thicknesses. During the deposition period of the experiment some PVK already has formed, leading to a non-zero starting thickness for the evaluation (see Fig. S1). We have taken the 3D-PVK peak at 31.4° as a measurement to estimate the initial thickness. For that we used the maximum integrated intensity (316 cps°) and α from that 31.4° peak at the end of the annealing experiment (1.44 cps° per nm) to calculate $d_{PVK,0}$ to be 219 nm. The influence of the starting thickness is discussed later. The final PVK thickness was determined *via* SEM (see Fig. S9) to around 1850 nm. In Table S3 all initial parameters for all experiments are listed. Fig. 7 shows the calculation results. In the upper graph the measured (dotted) data are shown for the PVK (blue) and FAI (red). The solid lines represent the fits with the optimised diffusion coefficient $D = 4.66 \times 10^{-12}$ cm^2 s^{-1}. The lower graph shows the simulated perovskite growth according to eqn (12) as a solid line. Here, the dotted line represents an extrapolation, as if the condition of unlimited FAI and PbI_2 supply would be guaranteed. It can be seen, that the final measured SEM PVK thickness (1850 nm) and the extrapolated PVK thickness (1930 nm) are in good agreement, supporting the reliability of our calculated diffusion coefficient. This resulting diffusion coefficient was used for the Arrhenius plot.

The evaluation has been performed for all experiments from 90 °C to 120 °C in 5 °C steps. The Arrhenius plot in Fig. 8 shows the diffusion coefficients of all isothermal annealing experiments as a function of inverse temperature. Note, that the real substrate temperature is estimated 16 K below the nominal temperature, due to the temperature difference between front and back side of the sample (following the calibration procedure detailed in the SI). It can be seen, that all points are following the linear trend. The resulting activation energy is 0.84 eV and the preexponential factor 3.63 cm^2 s^{-1}. The error bars were acquired by calculating the Gaussian error propagation. For the Gaussian error propagation, the individual uncertainties were determined from the maximum deviation of the evaluated parameters c_s, $d_{PVK,0}$, and t_0, which will be discussed in the next chapter. This results in an uncertainty of the activation energy of ±0.18 eV. Due to the logarithmic scale, the error for the preexponential factor $\Delta \ln(D_0)$ is asymmetric. The uncertainty interval is $D_0 \in [1.20 \times 10^{-2}; 1.10 \times 10^{+3}]$ cm^2 s^{-1}. Fig. 3 shows the *in situ* diffractograms of the 3D PVK peak at 31.4°

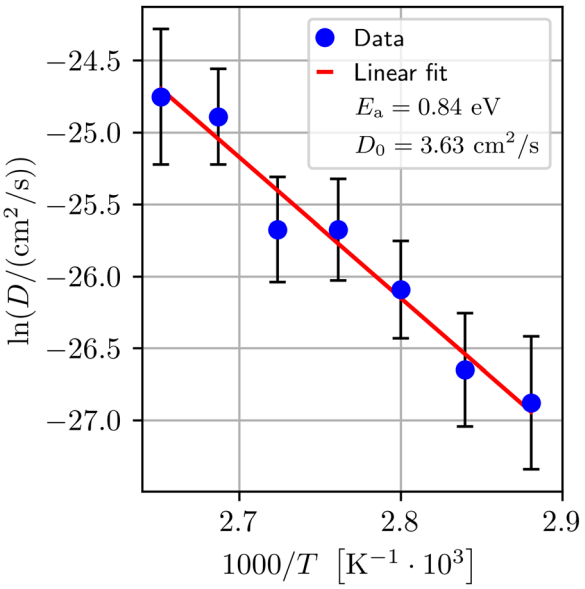

Fig. 8 Arrhenius plot with error bars of all seven experiments with c_s/c_0 = 80%. The calculated activation energy is E_a = 0.84 eV and the preexponential factor is D_0 = 3.63 cm^2 s^{-1}. The temperature data are corrected to the calibrated values as described in the text.

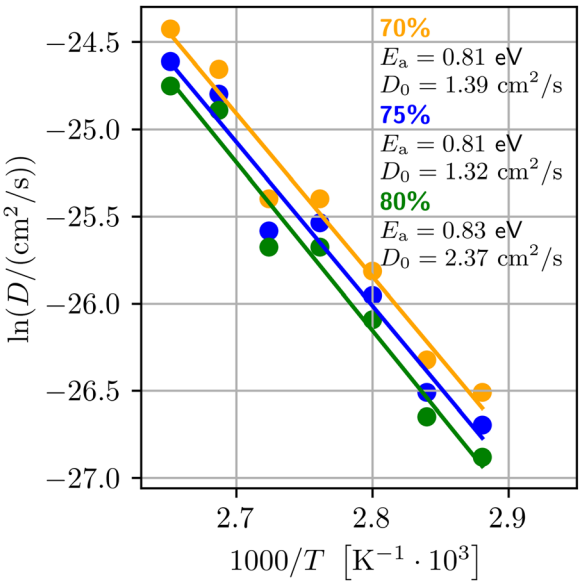

Fig. 9 Arrhenius plot for c_s/c_0 of 70%, 75% and 80% to estimate uncertainty due to saturation concentration variation.

for all nominal temperatures, together with the adjusted t_{end}. As expected, the needed time to complete the diffusion decreases with higher annealing temperature. Similar to Fig. 7, the fit results of the remaining temperatures are shown in Fig. S13.

5. Discussion

In the following, we will check how strongly the chosen boundary and starting conditions of our fitting procedure impact on the results, in order to estimate the error of our findings. Then, a comparison with literature values will be given.

5.1 Effect of saturation concentration c_s

Firstly, we will check how strongly the choice of the saturation concentration (70–80%) impacts on the results. For this, we conducted the same calculation with a normalised saturation concentration of 70%, 75% and 80%. The results are shown in Fig. 9. An increase in c_s/c_0 leads to lower diffusion coefficients in the chosen temperature interval. The correlation between saturation concentration and diffusion coefficient is shown in Fig. 10. A fit-error-minimum band is seen, indicating that the c_s and D cannot be fitted simultaneously. Because of that, c_s was estimated with an additional experiment and set to 80%, as discussed in Section 3.2. By varying the normalised saturation concentration between 70 and 80%, the activation energy changes by 0.02 eV (2.4%). Additionally, D_0 differs within the same order of magnitude due to the difference in E_a (slope). Variations in the saturation concentration only weakly affect the concentration gradient at the PVK|PbI_2 interface and therefore have a negligible influence on the FAI flux for sufficiently

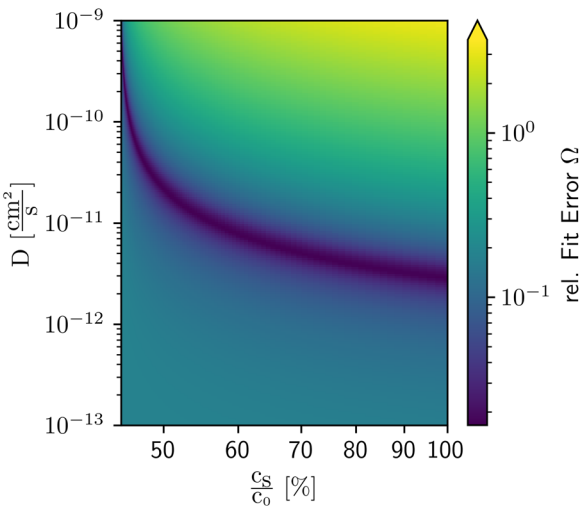

Fig. 10 Relative fit error Ω in dependency of the diffusion coefficient D and the normalised saturation concentration, with a constant minimum concentration c_m. No global minimum is seen, but a "minimum-band". This implies a correlation between c_s and D.

thick perovskite layers, leaving the extracted diffusion coefficients and thus Arrhenius parameters almost unchanged.

5.2 Effect of different PVK starting thickness $d_{PVK,0}$

To analyse the effect of a different starting PVK thickness $d_{PVK,0}$, the same evaluations were done with a starting thickness of 100 and 500 nm. The saturation concentration was set to c_s/c_0 = 80%. The Arrhenius plots are shown in Fig. S10. Choosing a smaller $d_{PVK,0}$ results in no change in the activation energy and preexponential factor. Upon increasing the starting thickness to 500 nm, E_a and D_0 increase by 0.05 eV and 8.82 cm^2 s^{-1}, respectivly. While a smaller initial perovskite thickness increases

the early-time FAI flux, the growth rate decreases at longer annealing times following the characteristic $\sqrt{t}$ behaviour, such that variations in the starting thickness do not significantly affect the diffusion coefficient obtained from long-time kinetics.

5.3 Effect of different starting times t_0

Also, a variation of the starting time t_0 was performed. For that, besides the used 10 min, also 8 and 12 min were tested, which means starting the fitting procedure one measurement point earlier or later, respectively. The results can be seen in Fig. S12. A minor decrease in activation energy (0.04 eV) can be seen between 10 and 12 min, whereas E_a increases by 0.07 eV between 10 and 8 min. This also decreases (increases) the preexponential factor by a factor of 4 (10) between 10 and 12 min (8 min). Shifting the effective start time results in a horizontal displacement of the diffusion-controlled PVK growth curve but has only a minor impact on the final perovskite thickness at long annealing times, where the growth rate is low.

5.4 Comparison with literature and contextualisation

The activation energy of 0.84 eV as determined by our experiments is comparable to values found at the chemically similar MA-based system. Eames *et al.* calculated the activation energy to 0.58 eV and 0.84 eV for I^- and MA^+, respectively, using their chronophotoampereometry measurement.[12] Futscher *et al.* published 0.29 eV for I^- and 0.39–0.90 eV for MA^+ *via* capacitance measurements.[13] It can be seen, that our value for E_a is close to the reported MA^+ activation energies.

In the SI we calculated the diffusion coefficient at 105 °C from Arrhenius parameters for selected publications.[12,13,31] Table S4 shows, that different measurements techniques result in diffusion coefficient discrepancies of multiple orders of magnitude (10^{-14}–10^{-9} cm^2 s^{-1}). Our value of 7.07×10^{-12} cm^2 s^{-1} is located within that interval, verifying the comparability of both chemical similar organic A-cations.

First principle calculation report migration barriers for halides and A-cations in the range of 0.44–0.48 eV (I^-), 0.57 eV (MA^+), and 0.61 eV (FA^+).[11] The small difference between MA^+ and FA^+ highlights the chemical similarity of the organic A-site cations. Additionally, Ghasemi *et al.* performed experiments to extract diffusion parameters for bulk and grain boundary diffusion. They reported lower activation energies for GB diffusion (0.46–0.57 eV) compared to bulk diffusion (0.61–0.74 eV).[32] Also, a recently published work by Siegert *et al.* utilizes *in situ* XRD measurements to determine activation energies for the diffusion of I^- into $MAPbBr_3$ (0.32 eV) and Br^- into $MAPbI_3$ (0.59 eV). Their model makes use of the Boltzmann–Matano approach combined with Rietveld refinement of the perovskite diffraction peaks.[33] A similar model was used by Wollstadt *et al.* to obtain diffusion parameters in oxide perovskites utilizing *in situ* XRD.[34] Overall, the activation energies obtained in our work are slightly higher than most previous reported values. This difference can be rationalized by the distinct experimental configuration and diffusion geometry employed here, which differs from commonly investigated systems.

Our comparatively high preexponential factor D_0 arises from defect-mediated transport and the high defect densities characteristic of halide perovskites[35] and therefore represents effective transport prefactors rather than bulk diffusion parameters.[36] Futscher *et al.* give values for the diffusion coefficient at 300 K, which translates (together with the E_a values) to values for D_0 in the range of 10^{-6} to 10^3 cm^2 s^{-1} for the MA^+ ions. Ghasemi *et al.* determined preexponential factors on the order of 10^{-3} cm^2 s^{-1} for bulk and 10^{-1} cm^2 s^{-1} for grain boundary diffusion and are thus within the same range as values from this work.[32]

For future solar cell device upscaling approaches, a low annealing time is desired. For example, for a τ = 1 min annealing step, the necessary annealing temperature can be estimated with our results. Preparing a L = 2 μm thick absorber and utilizing $D = \frac{L^2}{\tau}$, a diffusion coefficient of $D = 6.67 \times 10^{-10}$ cm^2 s^{-1} is necessary. Performing an extrapolation using the Arrhenius parameters, a temperature of 168 °C can be calculated. Considering the low annealing time, no significant degradation effects should apply to the film.

6. Summary

We conducted experiments to quantify the FAI diffusion through the PVK layer in the diffusion system PbI_2–PVK–FAI. For this purpose, we deposited *via* sequential deposition a stack of pure PbI_2 + FAI layers *via* sequential deposition. A following isothermal annealing step allowed us to determine the diffusion coefficient for the chosen annealing temperature by a mathematical model, utilising the *in situ* XRD system. Comparing data from experiments conducted at different annealing temperatures allows to make an Arrhenius plot and determined the preexponential factor D_0 and activation energy E_a to 1.20×10^{-2}–$1.10 \times 10^{+3}$ cm^2 s^{-1} and 0.84 ± 0.18 eV, respectively. This work leads the way to advanced insight into the diffusion and perovskite growth for sequential deposition and annealing processes. Our goal for the future is to analyse more material systems and quantify the effect by adding different ions into the $FAPbI_3$ system. For example, caesium and chloride are said to increase the diffusivity and thus perovskite growth.[8,37]

Author contributions

T. S., R. S., and P. P. developed the experimental procedure. T. S. and M. M. mathematically described the used diffusion model. The base code was created by M. S. and T. S. expanded it. P. P. guided the scientific progress. T. S. deposited the films and evaluated the experiments. T. S., M. M., R. S., and P. P. discussed and interpreted the results. T. S. wrote the main manuscript.

Conflicts of interest

There are no conflicts to declare.

Data availability

Data for this article, including the XRD and experimental deposition/annealing data are available at https://cloud.uni-halle.de/s/0fmJ80Aag8T42Dt.

Supplementary information (SI) containing XRD colormaps, fit plots and fit parameters. See DOI: https://doi.org/10.1039/d5cp03252k.

Acknowledgements

The German Research Foundation (DFG) under contract number SCHE-1745/9-1 and the Spanish Ministry of Science, Innovation and Universities under contract number (CNS2024-154809) provided gratefully acknowledged financial support. M. M. acknowledges funding by BMWK/PTJ (Project PVKIS) under contract number (03EE1206D). Funding for open access publishing: Universidad Pablo de Olavide/CBUA.

References

1 A. Kojima, K. Teshima, Y. Shirai and T. Miyasaka, Organometal Halide Perovskites as Visible-Light Sensitizers for Photovoltaic Cells, *J. Am. Chem. Soc.*, 2009, **131**(17), 6050–6051.
2 Best Research-Cell Efficiency Chart|Photovoltaic Research| NREL, [cited 2025 June 27]. Available from: https://www.nrel.gov/pv/cell-efficiency.
3 J. H. Lee, B. S. Kim, J. Park, J. W. Lee and K. Kim, Opportunities and Challenges for Perovskite Solar Cells Based on Vacuum Thermal Evaporation, *Adv. Mater. Technol.*, 2023, **8**(20), 2200928.
4 S. R. Bae, D. Y. Heo and S. Y. Kim, Recent progress of perovskite devices fabricated using thermal evaporation method: perspective and outlook, *Mater. Today Adv.*, 2022, **14**, 100232.
5 J. Feng, Y. Jiao, H. Wang, X. Zhu, Y. Sun and M. Du, *et al.*, High-throughput large-area vacuum deposition for high-performance formamidine-based perovskite solar cells, *Energy Environ. Sci.*, 2021, **14**(5), 3035–3043.
6 R. Vidal, J. A. Alberola-Borràs, S. N. Habisreutinger, J. L. Gimeno-Molina, D. T. Moore and T. H. Schloemer, *et al.*, Assessing health and environmental impacts of solvents for producing perovskite solar cells, *Nat. Sustain.*, 2020, **4**(3), 277–285.
7 M. Liu, M. B. Johnston and H. J. Snaith, Efficient planar heterojunction perovskite solar cells by vapour deposition, *Nature*, 2013, **501**(7467), 395–398.
8 H. Li, J. Zhou, L. Tan, M. Li, C. Jiang and S. Wang, *et al.*, Sequential vacuum-evaporated perovskite solar cells with more than 24% efficiency, *Sci. Adv.*, 2022, **8**(28), eabo7422.
9 Y. Vaynzof, The Future of Perovskite Photovoltaics---Thermal Evaporation or Solution Processing?, *Adv. Energy Mater.*, 2020, **10**(48), 2003073.
10 W. Tress, N. Marinova, T. Moehl, S. M. Zakeeruddin, M. K. Nazeeruddin and M. Grätzel, Understanding the rate-dependent *J–V* hysteresis, slow time component, and aging in $CH_3NH_3PbI_3$ perovskite solar cells: the role of a compensated electric field, *Energy Environ. Sci.*, 2015, **8**(3), 995–1004.
11 J. Haruyama, K. Sodeyama, L. Han and Y. Tateyama, First-Principles Study of Ion Diffusion in Perovskite Solar Cell Sensitizers, *J. Am. Chem. Soc.*, 2015, **137**(32), 10048–10051.
12 C. Eames, J. M. Frost, P. R. F. Barnes, B. C. O'Regan, A. Walsh and M. S. Islam, Ionic transport in hybrid lead iodide perovskite solar cells, *Nat. Commun.*, 2015, **6**(1), 7497.
13 M. H. Futscher, J. M. Lee, L. McGovern, L. A. Muscarella, T. Wang and M. I. Haider, *et al.*, Quantification of ion migration in $CH_3NH_3PbI_3$ perovskite solar cells by transient capacitance measurements, *Mater. Horiz.*, 2019, **6**(7), 1497–1503.
14 W. M. Haynes, *CRC Handbook of Chemistry and Physics*, CRC Press, 97th edn, 2017.
15 A. A. Petrov, E. A. Goodilin, A. B. Tarasov, V. A. Lazarenko, P. V. Dorovatovskii and V. N. Khrustalev, Formamidinium iodide: crystal structure and phase transitions, *Acta Crystallogr., Sect. E: Crystallogr. Commun.*, 2017, **73**(Pt 4), 569–572.
16 T. Burwig and P. Pistor, Reaction kinetics of the thermal decomposition of $MAPbI_3$ thin films, *Phys. Rev. Mater.*, 2021, **5**(6), 065405.
17 P. Pistor, T. Burwig, C. Brzuska, B. Weber and W. Fränzel, Thermal stability and miscibility of co-evaporated methyl ammonium lead halide ($MAPbX_3$, X = I, Br, Cl) thin films analysed by in situ X-ray diffraction, *J. Mater. Chem. A*, 2018, **6**(24), 11496–11506.
18 K. L. Heinze, T. Schulz, R. Scheer and P. Pistor, Structural Evolution of Sequentially Evaporated $(Cs,FA)Pb(I,Br)_3$ Perovskite Thin Films via In Situ X-Ray Diffraction, *Phys. Status Solidi A*, 2024, **221**(3), 2300690.
19 S. Hartnauer, L. A. Wägele, F. Syrowatka, G. Kaune and R. Scheer, Co-evaporation process study of $Cu_2ZnSnSe_4$ thin films by in situ light scattering and in situ X-ray diffraction, *Phys. Status Solidi A*, 2015, **212**(2), 356–363.
20 D. Zheng, P. Volovitch and T. Pauporté, What Can Glow Discharge Optical Emission Spectroscopy (GD-OES) Technique Tell Us about Perovskite Solar Cells?, *Small Methods*, 2022, **6**(11), 2200633.
21 S. P. Harvey, Z. Li, J. A. Christians, K. Zhu, J. M. Luther and J. J. Berry, Probing Perovskite Inhomogeneity beyond the Surface: TOF-SIMS Analysis of Halide Perovskite Photovoltaic Devices, *ACS Appl. Mater. Interfaces*, 2018, **10**(34), 28541–28552.
22 D. H. Fabini, C. C. Stoumpos, G. Laurita, A. Kaltzoglou, A. G. Kontos and P. Falaras, *et al.*, Reentrant Structural and Optical Properties and Large Positive Thermal Expansion in Perovskite Formamidinium Lead Iodide, *Angew. Chem., Int. Ed.*, 2016, **55**(49), 15392–15396.
23 D. Lin, J. Fang, X. Yang, X. Wang, S. Li and D. Wang, *et al.*, Modulating the Distribution of Formamidinium Iodide by Ultrahigh Humidity Treatment Strategy for High-Quality Sequential Vapor Deposited Perovskite, *Small*, 2023, 2307960.
24 N. Nadaud, N. Lequeux, M. Nanot, J. Jové and T. Roisnel, Structural Studies of Tin-Doped Indium Oxide (ITO) and $In_4Sn_3O_{12}$, *J. Solid State Chem.*, 1998, **135**(1), 140–148.

25 T. Yokoyama, S. Ohuchi, E. Igaki, T. Matsui, Y. Kaneko and T. Sasagawa, An Efficient ab Initio Scheme for Discovering Organic–Inorganic Hybrid Materials by Using Genetic Algorithms, *J. Phys. Chem. Lett.*, 2021, **12**(8), 2023–2028.
26 K. L. Heinze, P. Wessel, M. Mauer, R. Scheer and P. Pistor, Stoichiometry dependent phase evolution of co-evaporated formamidinium and cesium lead halide thin films, *Mater. Adv.*, 2022, **3**(23), 8695–8704.
27 M. Bukleski, S. Dimitrovska-Lazova and S. Aleksovska, Vibrational spectra of methylammonium iodide and formamidinium iodide in a wide temperature range, *Maced. J. Chem. Chem. Eng.*, 2019, **38**(2), 237–252.
28 S. Wang, D. B. Mitzi, C. A. Feild and A. Guloy, Synthesis and Characterization of $[NH_2C(I){:}NH_2]_3MI_5$ (M = Sn, Pb): Stereochemical Activity in Divalent Tin and Lead Halides Containing Single.ltbbrac.110.rtbbrac. Perovskite Sheets, *J. Am. Chem. Soc.*, 1995, **117**(19), 5297–5302.
29 B. D. Cullity, *Elements Of X Ray Diffraction*, Addison-Wesley Publishing Company, Inc., 1956, p. 531, Available from: https://archive.org/details/elementsofxraydi030864mbp.
30 M. Birkholz and P. F. Fewster, High-Resolution X-ray Diffraction, *Thin Film Analysis by X-Ray Scattering*, John Wiley & Sons, Ltd, 2005, pp. 297–341. Available from: https://onlinelibrary.wiley.com/doi/abs/10.1002/3527607595.ch7.
31 A. Senocrate, I. Moudrakovski, G. Y. Kim, T. Y. Yang, G. Gregori and M. Grätzel, *et al.*, The Nature of Ion Conduction in Methylammonium Lead Iodide: A Multimethod Approach, *Angew. Chem.*, 2017, **129**(27), 7863–7867.
32 M. Ghasemi, B. Guo, K. Darabi, T. Wang, K. Wang and C. W. Huang, *et al.*, A multiscale ion diffusion framework sheds light on the diffusion–stability–hysteresis nexus in metal halide perovskites, *Nat. Mater.*, 2023, **22**(3), 329–337.
33 T. Siegert, P. Pahwa, M. Griesbach, F. J. Kahle, H. Oberhofer and A. Köhler, *et al.*, Modelling Thermal Halide Exchange of Perovskite Powders With and Without $BMIMBF_4$ From an Interdiffusion Perspective, *Adv. Funct. Mater.*, 2025, e10920.
34 S. Wollstadt, R. A. De Souza and O. Clemens, Kinetic Study of the Interdiffusion of Fluorine and Oxygen in the Perovskite-Type Barium Ferrate System $BaFeO_{2.5-x}F_{2x}$, *J. Phys. Chem. C*, 2021, **125**(4), 2287–2298.
35 A. Walsh, D. O. Scanlon, S. Chen, X. G. Gong and S. H. Wei, Self-Regulation Mechanism for Charged Point Defects in Hybrid Halide Perovskites, *Angew. Chem., Int. Ed.*, 2015, **54**(6), 1791–1794.
36 P. Shewmon, Diffusion in Solids, in *Diffusion in Solids*, ed. P. Shewmon, Springer International Publishing, Cham, 2016, DOI: 10.1007/978-3-319-48206-4_1.
37 J. Yan, J. Nespoli, R. K. Boekhoff, H. Wang, T. Gort and M. Tijssen, *et al.*, Chloride-improved crystallization in sequentially vacuum-deposited perovskites for p–i–n perovskite solar cells, *Sustainable Energy Fuels*, 2025, **9**(10), 2729–2737.